

Additive Manufacturing

A simple and efficient manufacturing design method for additive manufacturing with multiple printing sizes

--Manuscript Draft--

Manuscript Number:	ADDMA-D-20-00037
Article Type:	Research Paper
Keywords:	additive manufacturing; Computer aided design; Implicit method; Adaptive refinement mesh
Corresponding Author:	Junseok Kim Korea University Seoul, Korea, Republic of
First Author:	Yibao Li
Order of Authors:	Yibao Li Xia Qing Zhengyuan Shi Bingheng Lu Junseok Kim
Abstract:	Additive manufacturing has been successfully used in the manufacturing industry and has become an important topic of scientific research. Optimization among the manufacturing time, cost, and accuracy has been important in this field. In this study, an efficient manufacturing method is designed for additive manufacturing with multiple printing sizes, which involves a printer with several nozzles. This method can be extended to use the octree adaptive mesh method and is much easier to implement. The proposed algorithm partitions the internal area of the model into modules with different accuracies based on the requirements such as distance and stress. Additionally, porous structures can be used to replace the inside modules because of their special properties such as higher rigidity and lightweight. Multi-scale lightweight structures and porosity gradient structures are generated to further reduce the material weight without affecting the mechanical stability. The experimental results demonstrate that the proposed method can provide effective solutions for various additive manufacturing design problems.
Suggested Reviewers:	Dong J. Yoo Daejin University djyoo@daejin.ac.kr Derrick Dean Alabama State University ddean@alasu.edu Howon Lee Rutgers University howon.lee@rutgers.edu Min Liu Guangdong Institute of New Materials Lumin@gdas.gd.cn

February 28, 2020

Additive Manufacturing

Dear Editor:

Please consider the manuscript entitled “**A simple and efficient manufacturing design method for additive manufacturing with multiple printing sizes**” authored by Yibao Li, Qing Xia, Zhengyuan Shi, Bingheng Lu and Junseok Kim, which we are submitting for consideration for publication in **Additive Manufacturing**. We were fully involved in the study and preparation of the manuscript and that the material within has not been and will not be submitted for publication elsewhere. Along with the constructive comments of the reviewer concerning our manuscript (ADDMA_2020_401). We also respond point by point to the editor and reviewer’s comments as listed below.

Comments: Please consult a professional language service if you submit again. We will read the entire document and only consider publication-ready manuscripts.

Answer: The paper has been carefully revised by a professional language editing service to improve the grammar and readability.

Comments: *confusing first sentence

*awkward: The balance between time cost and manufacturing accuracy has been the primary problem to be solved.

*awkward: Matching with the different nozzles, the algorithm separates the internal area of the model into modular with different accuracy according to the requirement information (e.g., distance field, stress field).

Answer: The sentences have been modified as “Optimization among the manufacturing time, cost, and accuracy has been important in this field. In this study, an efficient manufacturing method is designed for additive manufacturing with multiple printing sizes, which involves a printer with several nozzles.”

We look forward to hearing from you with regard to the status of this manuscript and welcome your esteemed comments.

The corresponding author's information follows: Email is cfdkim@korea.ac.kr and website is <http://math.korea.ac.kr/~cfdkim/>

Sincerely,

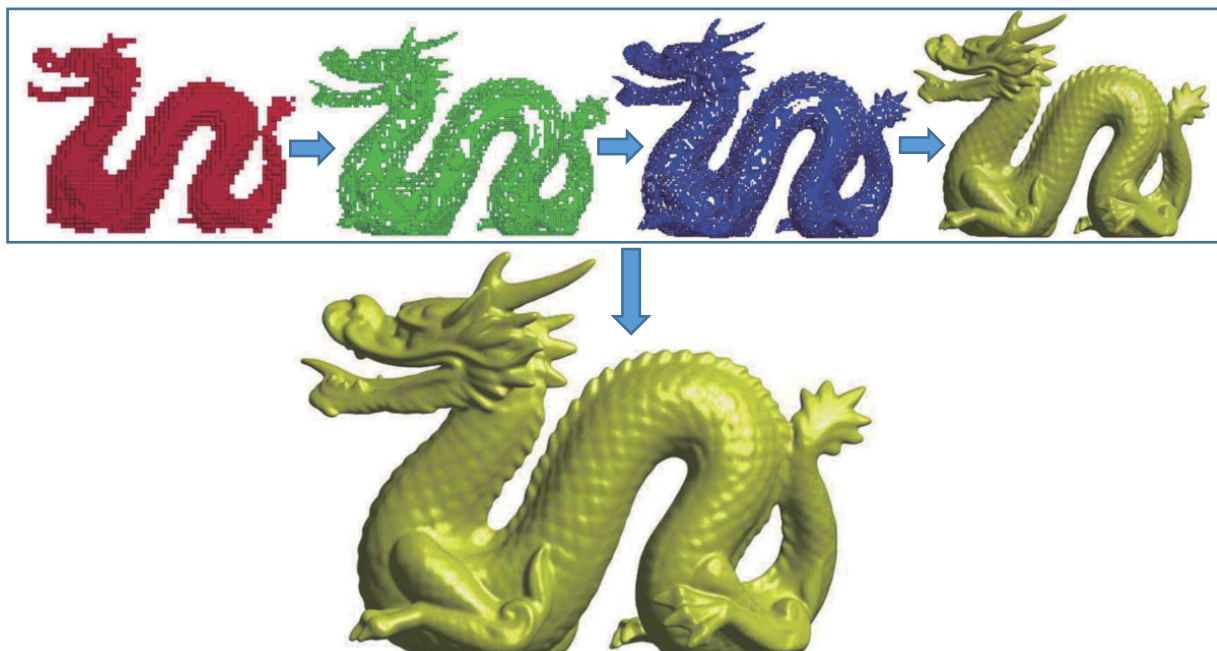
Junseok Kim

Professor of Department of Mathematics

Korea University

1 **Highlights**
2
3
4
5
6
7
8
9

- We propose an efficient and robust computer-aided design method for additive manufacturing.
 - A heuristic multi-nozzle printing method is proposed to control accuracy and efficiency of 3D printing.
 - Various tests were implemented to show the robustness and efficiency of our method.
- 10
11
12
13
14
15
16
17
18
19
20
21
22
23
24
25
26
27
28
29
30
31
32
33
34
35
36
37
38
39
40
41
42
43
44
45
46
47
48
49
50
51
52
53
54
55
56
57
58
59
60
61
62
63
64
65



1
2
3 1 A simple and efficient manufacturing design method for additive manufacturing
4 2 with multiple printing sizes
5
6

7 3 Yibao Li^a, Qing Xia^a, Zhengyuan Shi^a, Bingheng Lu^{b,c,d}, Junseok Kim^{e,*}
8

9 4 ^aSchool of Mathematics and Statistics, Xi'an Jiaotong University, Xi'an 710049, China
10 5 ^bCollaborative Innovation Center of High-End Manufacturing Equipment, Xi'an Jiaotong University, Xi'an 710049, China
11 6 ^cNational Institute of Additive Manufacturing, Xi'an 710049, China

12 7 ^dSchool of Mechanical Engineering, Dongguan University of Technology, Dongguan 523808, China
13 8 ^eDepartment of Mathematics, Korea University, Seoul 02841, Republic of Korea

14
15
16
17 9 **Abstract**

18 Additive manufacturing has been successfully used in the manufacturing industry and has become an important topic
19 of scientific research. Optimization among the manufacturing time, cost, and accuracy has been important in this field.
20 In this study, an efficient manufacturing method is designed for additive manufacturing with multiple printing sizes,
21 which involves a printer with several nozzles. This method can be extended to use the octree adaptive mesh method
22 and is much easier to implement. The proposed algorithm partitions the internal area of the model into modules
23 with different accuracies based on the requirements such as distance and stress. Additionally, porous structures can
24 be used to replace the inside modules because of their special properties such as higher rigidity and lightweight.
25 Multi-scale lightweight structures and porosity gradient structures are generated to further reduce the material weight
26 without affecting the mechanical stability. The experimental results demonstrate that the proposed method can provide
27 effective solutions for various additive manufacturing design problems.
28
29

30 10 **Keywords:** Additive manufacturing, Computer aided design, Implicit method, Adaptive refinement mesh
31
32

33
34 11 **1. Introduction**
35
36

37 Time cost and manufacturing efficiency are two key parameters in the field of additive manufacturing [1, 2]. The
38 relationship between time and manufacturing accuracy severely limits the development of additive manufacturing
39 technology [3, 4]. Various additive manufacturing methods have been invented and applied to practical production.
40 Direct ink writing technology was used to extend two-dimensional printing to three-dimensional space [5, 6, 7]. Un-
41 like other single-material printing methods, the authors in [8] used photopolymers as the build material and wax as
42 the support material, and they evaluated the building performance by constructing a benchmark model with a high-
43 resolution printing mode. Stereolithography and selective laser sintering utilize the characteristics of photopolymer
44

45 *Corresponding author
46 Email addresses: yibaoli@xjtu.edu.cn (Yibao Li), cfdkим@korea.ac.kr (Junseok Kim)
47 URL: <http://gr.xjtu.edu.cn/web/yibaoli> (Yibao Li), <http://math.korea.ac.kr/~cfdkim> (Junseok Kim)

1
2
3
4 materials to fabricate objects [9]. In fused deposition modeling (FDM), the refractory material is melted at a high
5 temperature and the model is built by stacking. Various methods for additive manufacturing have been consistently
6 developed and upgraded. Tao et al. [10] used functional materials to effectively perform nerve repair via rapid 3D
7 printing technology. Guba et al. [11] used additive manufacturing technologies for photochemical reaction engineer-
8 ing, which significantly reduced the time cost. Nguyen et al. [12] combined additive manufacturing and intraoperative
9 computed tomography for treating orbital fractures, which overcame the drawbacks of traditional treatment methods.
10
11 Yacob et al. [13] proposed an octree-based method to generate slice data. Several methods have also been developed
12 and applied without considering the adding materials [14]. Petrzalka et al. [15] proposed a subtractive process plan-
13 ning algorithm that is independent of specific tool paths. Kelly et al. [16] proposed a novel prototyping technology
14 using volume reconstruction. This method provided a novel approach for efficiency improvement in the manufacturing
15 industry.



44
45 Figure 1: Design results of a Stanford dragon of size 95.4mm × 68mm × 44.4mm. (a) Design results of four individual levels. (b) Combined
46 results of four levels.

47
48 In this work, a simple and efficient refinement mesh algorithm is proposed to design 3D models with highly robust
49 design performance and low time consumption. Unlike existing adaptive slicing algorithms [17, 18, 19, 20], the
50 proposed method is based on the signed distance or stress fields of additive manufacturing, which can ensure good
51 mechanical properties. The model generated using the proposed method is far more suitable for voxel/pixel based
52 additive manufacturing technology. As shown in Fig. 1(a), the entire Stanford-dragon is divided into four areas,
53 represented by red, green, blue, and yellow, respectively. From left to right, reduced manufacturing sizes were used to
54
55
56
57

1
 2
 3 36 design different areas. The entire volume composed of four areas has sufficiently high enough accuracy, as shown in
 4 37 Fig. 1(b). The calculation scale of this model is $95.4\text{mm} \times 68\text{mm} \times 44.4\text{mm}$, and the precision is 0.1mm . It is worth
 5 38 noting that the yellow part of Fig. 1(a) represents the area that needs to be built with the highest accuracy, and the
 6 39 resulting effect is shown in Fig. 1(b). The time cost and accuracy of the proposed method are compared with those of
 7 40 traditional computer-aided design methods in a subsequent section. Porous structures can be extensively used inside
 8 41 the model because of their special mechanical and biological properties [21, 22, 23, 24]. Various experimental tests
 9 42 have been performed for different structures to demonstrate the robustness and efficiency of the proposed method.
 10
 11
 12
 13
 14 The remainder of this paper is organized as follows. In Section 2, the proposed method is described. Section 3
 15
 16 43 presents the various numerical experiments conducted. Finally, the conclusions are presented in Section 4.
 17
 18
 19 45 **2. Methodology**
 20
 21 46 *2.1. Triply periodic minimal surface structures*
 22
 23 47 Triply periodic minimal surfaces (TPMS) are of special interest to materials scientists, physicist, mathematicians
 24 48 [25], and biologists [26, 27], because the geometry of TPMS significantly influences the physical properties of a
 25 49 material [28, 29, 30]. The TPMS structure is suitable in tissue engineering because of its robust physical stability
 26 50 [31]. The approximations of Schwarz primitive (P), Schwarz diamond (D), Schwarz gyroid (G), and Schwarz I-WP
 27 51 (I) surfaces are commonly used as follows [32]:
 28
 29
 30
 31
 32 $P(x, y, z) = \cos(2\pi x) + \cos(2\pi y) + \cos(2\pi z),$
 33
 34 $D(x, y, z) = \cos(2\pi x) \cos(2\pi y) \cos(2\pi z) - \sin(2\pi x) \sin(2\pi y) \sin(2\pi z),$
 35
 36 $G(x, y, z) = \sin(2\pi x) \cos(2\pi y) + \sin(2\pi z) \cos(2\pi x) + \sin(2\pi y) \cos(2\pi z),$
 37
 38 $I(x, y, z) = 2(\cos(2\pi x) \cos(2\pi y) + \cos(2\pi y) \cos(2\pi z) + \cos(2\pi z) \cos(2\pi x)) - (\cos(4\pi x) + \cos(4\pi y) + \cos(4\pi z)).$
 39
 40 52 In this work, a phase-field model [25] for TPMS is used as follows:
 41
 42
$$\phi_t = -\frac{F'(\phi)}{\epsilon^2} + \Delta\phi - \lambda \frac{\phi(1-\phi)}{\sqrt{2}\epsilon}. \quad (1)$$

 43
 44 53 Here, $F(\phi) = 0.25\phi^2(\phi-1)^2$ and λ is the mean value of the mean curvature defined as
 45
 46
$$\lambda = \frac{-\sqrt{2} \int_{\Omega} F'(\phi) dx}{\epsilon \int_{\Omega} \phi(1-\phi) dx}. \quad (2)$$

 47
 48 54 Under the triply periodic boundary condition for ϕ , triply periodic constant mean curvature surfaces are developed.
 49
 50 55 For example, the initial condition is set as $\phi^0 = \alpha + \beta P$ with the P surface. The other initial conditions for D , G ,
 51
 52 and I are analogously defined. For a given volume $V = \int_{\Omega} \phi^0 d\mathbf{x}$, $\alpha = (V - \beta \int_{\Omega} P d\mathbf{x}) / \int_{\Omega} d\mathbf{x} = V / \int_{\Omega} d\mathbf{x}$ can be
 53
 54 obtained, because $\int_{\Omega} P d\mathbf{x} = 0$. To restrict $\phi^0 \in [0, 1]$, the two conditions $\alpha + \beta \max(P) \leq 1$ and $\alpha + \beta \min(P) \geq 0$
 55
 56 should be satisfied. Here, $\max(P)$ and $\min(P)$ are the maximum and minimum values of P , respectively. Thus,
 57
 58 β is chosen as $\beta = \min((1-\alpha)/\max(P), -\alpha/\min(P))$. These surfaces can be approximated using the periodic
 59
 60
 61
 62
 63
 64
 65

constant mean curvature surface expansion to generate lightweight structures of tissue models, as shown in Fig. 2. It can be observed that the surfaces are smooth with a constant mean curvature. Additionally, smooth variation among different size structures is obtained, which has a significant influence on the construction of the multi-precision structure system. As shown in the bottom row of Fig. 2, continuous connections between structures with different sizes ensure the stability of the proposed model.

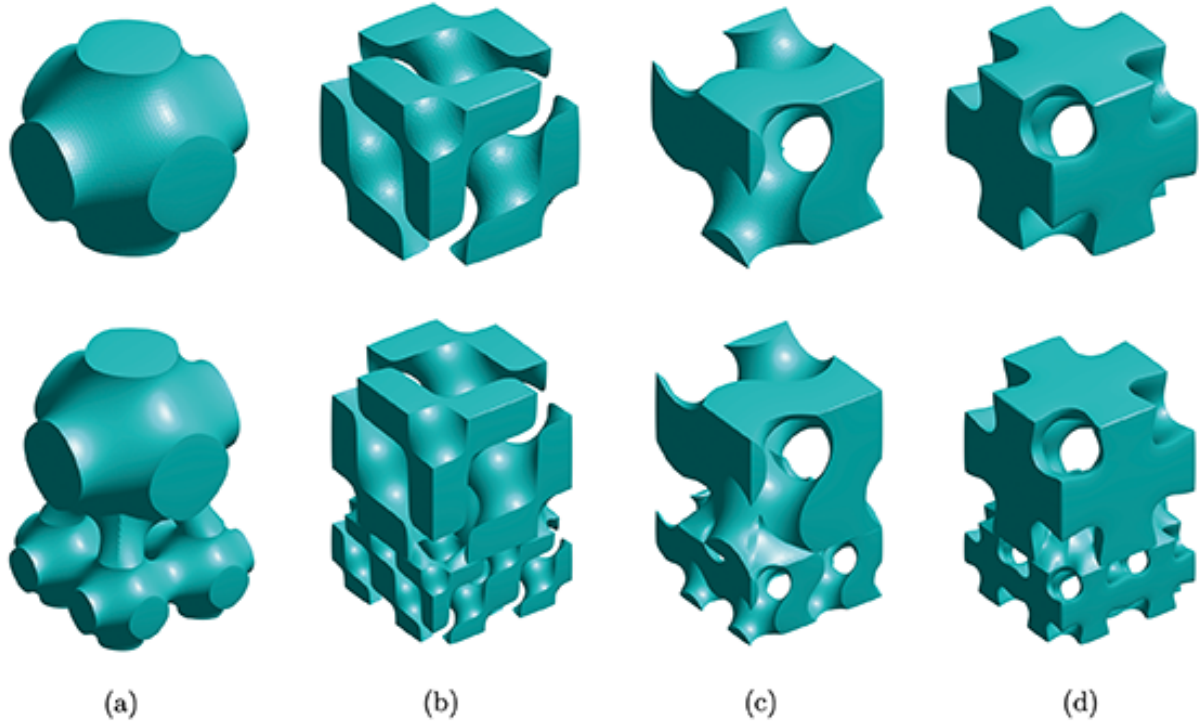


Figure 2: Triply periodic minimal surfaces. (a) Schwarz primitive (P), (b) Schwarz diamond (D), (c) Schwarz gyroid (G), (d) Schwarz I-WP (I) surface.

2.2. Signed distance field

Distance field is widely used in the domain of industrial design and additional material manufacturing [33]. A signed distance field contains the internal characteristics of the model, through which the manufacturing and designing accuracy, structural characteristics, and material properties at different distance levels can be controlled. As shown in Fig. 3(b), the domain is divided into four sub-domains, which are represented as white, cyan, green, and yellow. Suppose that a point \mathbf{x} is in the space Ω and the closest point to \mathbf{x} is denoted by $\bar{\mathbf{X}}$ in $\partial\Omega$. Then, the signed distance field is set as

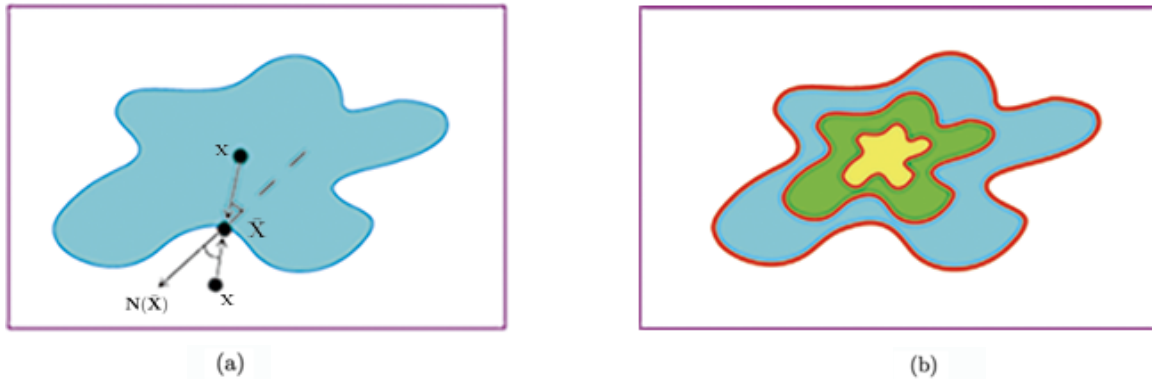
$$\phi(\mathbf{x}) = s(\mathbf{x})\bar{d}(\mathbf{x}), \quad (3)$$

where $\bar{d}(\mathbf{x}) = \|\mathbf{x} - \bar{\mathbf{X}}\|$, $s(\mathbf{x}) = \text{sign}((\mathbf{x} - \bar{\mathbf{X}}) \cdot \mathbf{N}(\bar{\mathbf{X}}))$, and \mathbf{N} is the outward normal vector at $\partial\Omega$, see Fig. 3(a). The interior and exterior zones are defined as positive and negative values, respectively. If $(\mathbf{x} - \bar{\mathbf{X}}) \cdot \mathbf{N}(\bar{\mathbf{X}}) \approx 0$, or

1
2
3 74 $\mathbf{N}(\bar{\mathbf{X}})$ involves noise, then $s(\mathbf{x})$ will also involve noise. The l_0 gradient regularization version is also considered:
4
5
6

$$\min_s \sum_{\mathbf{x} \in \Omega} g(\mathbf{x}) \|\nabla s\|_0, \quad (4)$$

75 where $g(\mathbf{x}) = \tanh(\bar{d}(\mathbf{x}) / (\sqrt{2}\xi))$ is a weighted function and ξ is a parameter related to thickness. The function is
9 almost zero near the data set and non-negative elsewhere. Further details can be found in our previous paper [25].
10
11



25
26 Figure 3: Graphical illustration of signed distance field. (a) Schematic to distinguish the external and internal points of the model in the entire
27 space. (b) Filled contours. Cyan, green, and yellow represent the domains with signed distances [0.5 1], [0.25 0.5] and [0 0.25], respectively.
28
29
30
31

77 2.3. Stress field

32 The distribution of stress fields in the model is important in additive manufacturing. Based on the stress field, the
33 points at which a material or structure with high bearing capacity is needed and those at which less material can be
34 used to reduce the weight of the model, can be deduced, as explained in [34, 35]. In order to obtain the stress field
35 distribution, the stress equilibrium differential equation must be solved:
36
37

$$38 \quad (\lambda + \mu) \nabla(\nabla \cdot \mathbf{u}) + \mu \nabla^2 \mathbf{u} + \mathbf{F} = 0 \quad (5)$$

41 Here, λ and μ are parameters, \mathbf{u} is the displacement vector, and \mathbf{F} is the body force per unit volume. Figure 4
42 shows the stress field. It is assumed that the material is general anisotropic linear elastic. Forces of equal magnitude
43 and opposite direction to the upper and lower sides of the model are considered; the warmer the color, the greater the
44 stress value.
45
46

47 2.4. Proposed algorithm

51 The objective of the proposed method is to adaptively generate models with strong mechanical properties based
52 on the signed distance field or stress field. The input 3D model is voxelized and the distances of the voxels on the
53 outer surface are set to zero. If a voxel is inside the model, it has a positive distance which is calculated from the
54 minimal distance between the voxel on the boundary; otherwise, it has a negative distance. $[0, L]$ is separated into
55 several sub-intervals or levels, where L is the largest positive distance. The voxels at each level are then considered
56
57

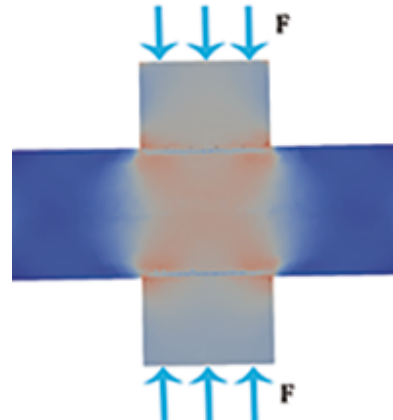


Figure 4: Distribution of stress field. The upper and lower sides of the model are subjected to the force of \mathbf{F} , respectively. The warm and cold colors represent regions with high and low stress, respectively.

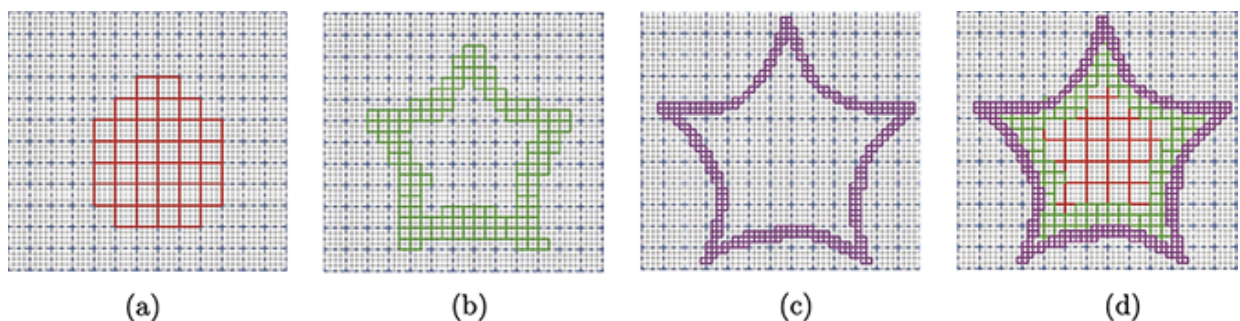


Figure 5: (a)–(c) Mesh structures of levels 1, 2 and 3, respectively. (d) Mesh structures of all three levels.

1
 2
 3 to be printed with the same accuracy. Here, the size of the voxel at each level should be specified; the larger distance,
 4 the larger the size. In order to explain the algorithm, first, the mesh structures of the two-dimensional Star-model are
 5 shown in Fig. 5. Figure 5(a)–(c) show the individual mesh structures of the three respective levels, and Fig. 5(d)
 6 shows their combination. Let $\Omega = (0, L_x) \times (0, L_y) \times (0, L_z)$ in three-dimensional space. Let N_x, N_y and N_z be
 7 positive integers, and $h = L_x/N_x = L_y/N_y = L_z/N_z$ be the uniform mesh size. Let ϕ_{ijk} be the approximation
 8 of $\phi((i-1)h + 0.5h, (j-1)h + 0.5h, (k-1)h + 0.5h)$. We introduce a hierarchy of increasingly finer grids,
 9 $\Omega_0, \Omega_1, \dots, \Omega_S$, restricted to subspaces with increasingly higher accuracy. Let $h_S = c \cdot h$ be the minimal length
 10 of domain Ω_S and c be a positive integer. Then, the length of domain Ω_s is set as $h_s = 2^{S-s}h_S = 2^{S-s}c \cdot h$, for
 11
 12
 13
 14
 15
 16 $s = 0, \dots, S$.

$$\hat{N}_x = N_x/(2^S c), \quad \hat{N}_y = N_y/(2^S c), \quad \hat{N}_z = N_z/(2^S c), \quad (6)$$

17
 18 where \hat{N}_x, \hat{N}_y , and \hat{N}_z represent the number of coarse mesh grids in each direction. Let d_s be the conditional
 19 thresholds such as distance or stress value. For each small domain of the subspace Ω_s , we can count the number of
 20 points by which the signed distance value is greater than d_s as:

$$\sum_{i=i_b}^{i_b+2^{S-s}c-1} \sum_{j=j_b}^{j_b+2^{S-s}c-1} \sum_{k=k_b}^{k_b+2^{S-s}c-1} f(\phi_{ijk}, d_s). \quad (7)$$

21
 22 Here, $f(x, y) = 0$, if $x < y$; otherwise, $f(x, y) = 1$. i_b, j_b , and k_b are the indexes of each small domain in subspace
 23
 24 Ω_s :

$$i_b = 1 + \sum_{m=0}^s (i_m - 1)2^{S-m}c, \quad j_b = 1 + \sum_{m=0}^s (j_m - 1)2^{S-m}c, \quad k_b = 1 + \sum_{m=0}^s (k_m - 1)2^{S-m}c, \quad (8)$$

25
 26 where $\mathbf{i} = [i_0, i_1, \dots, i_s], \mathbf{j} = [j_0, j_1, \dots, j_s]$ and $\mathbf{k} = [k_0, k_1, \dots, k_s]$ are three integer vectors. We refine the mesh
 27
 28 grid based on the center point of every small domain. The center of Ω_s is defined as:

$$C_x = (i_b - 1)h + 0.5h_s, \quad C_y = (j_b - 1)h + 0.5h_s, \quad C_z = (k_b - 1)h + 0.5h_s. \quad (9)$$

29
 30 If the judgment conditions are satisfied, box elements with h_s accuracy are generated in the subspaces. Otherwise,
 31 the coarse space is divided into eight fine subspaces and the previous step is repeated. The entire algorithm is divided
 32
 33 into two steps, as shown in Fig. 6.

34
 35 • Step 1 : Calculate the location (C_x, C_y, C_z) of the central point in each box and generate the lightweight struc-
 36 ture in the corresponding box.

37
 38 • Step 2 : Refine the mesh grids based on a judgement on whether to stratify according to Condition 2. If the
 39 condition holds, s is updated and the next grid level is refined for recursive computation. Otherwise, the current loop
 40 is continued, and (i_b, j_b, k_b) is updated. Here, two judgement conditions are defined:

41
 42 • Condition 1 : $\sum_{i=i_b}^{i_b+2^{S-s}c-1} \sum_{j=j_b}^{j_b+2^{S-s}c-1} \sum_{k=k_b}^{k_b+2^{S-s}c-1} f(\phi_{ijk}, d_s) = (2^{S-s}c)^3$
 43
 44 • Condition 2 : $s \leq S$

1
 2
 3
 118 The filtering space size can be selected adaptively with multiple printing sizes. Based on Fig. 6, it is worth pointing
 4
 5
 119 out that our adaptive mesh algorithm can realize manufacturing with an arbitrary number of levels by considering the
 6
 7
 accuracy of 3D printer nozzles in engineering applications.
 8
 9

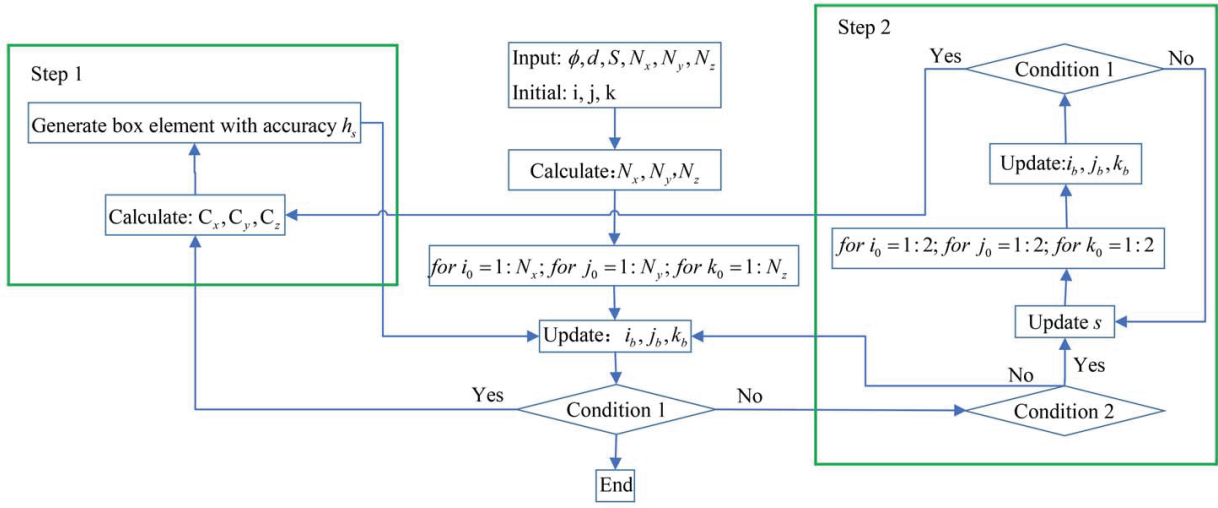


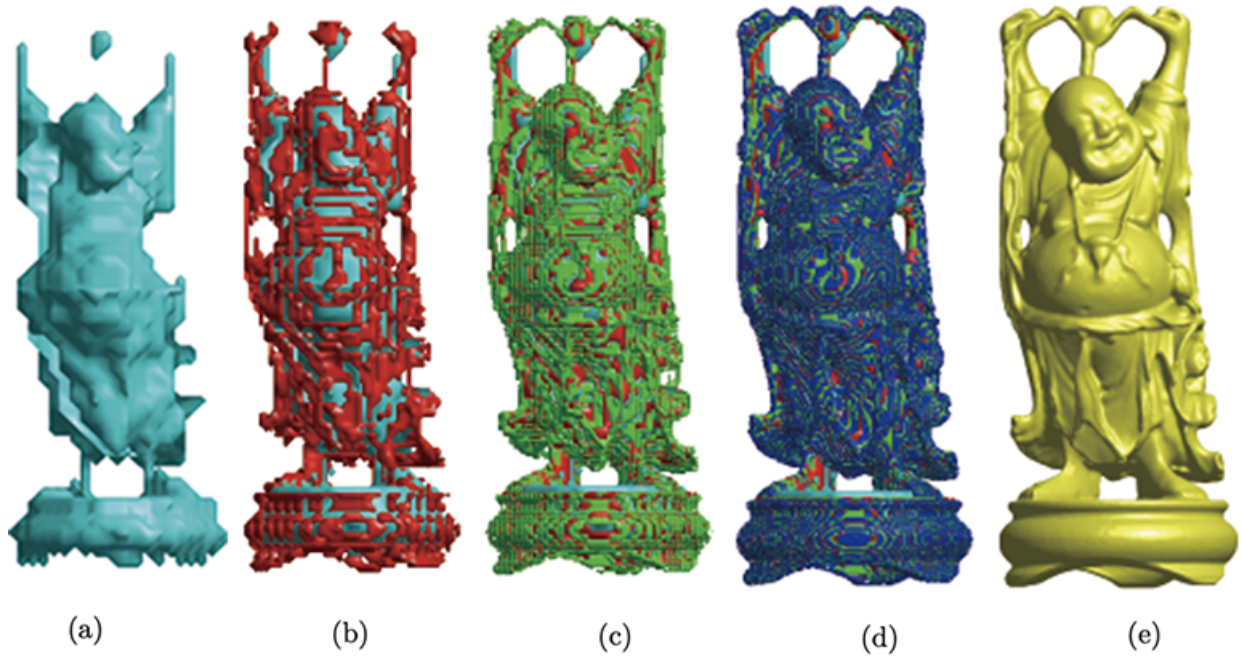
Figure 6: Schematic for developing adaptive refinement mesh algorithm.

3. Experimental tests

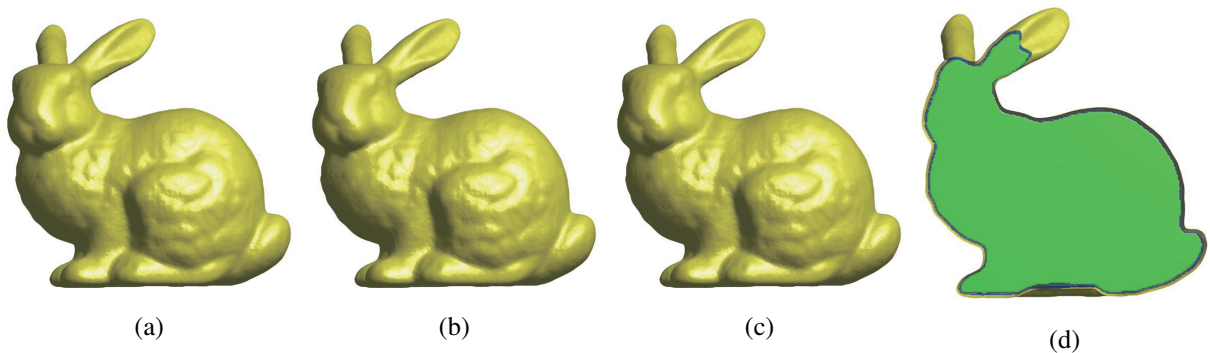
120
 121 Figure 7 shows multiple manufacturers for Happy Buddha. It is clear that only a small computational time is
 122 needed to create the parts that form the majority of the total volume. The signed distance function is used to control
 123 the thickness of each level. On the other hand, the accuracy of the model remains sufficiently high. It must be noted
 124 that this method is suitable for coupling multiple materials and structures while ensuring accuracy and efficiency.
 125

126 Considering the efficiency and accuracy of fabrication, the obtained models are compared using uniform printer
 127 nozzles and the adaptive printer nozzles shown in Fig. 8. The size of the model in Fig. 8 is 98mm × 103.2mm ×
 128 78mm. The smallest size of the printer nozzle is 0.1mm. The uniform size is used in Fig. 8(a), while the third and
 129 sixth levels are used in Fig. 8(b) and (c), respectively. Figure 8(d) shows the cut view of the model, which is obtained
 130 using three levels. The results for uniform and adaptive printer nozzles are clearly shown to be in good agreement.
 131

132 Some researchers have compared the efficiency of adaptive mesh algorithm with that of the traditional method
 133 [36, 37, 38, 39] and achieved good results. Compared to these results, our proposed method with multi-level design
 134 significantly reduces the time consumption. The volume portion of the manufacturing element is calculated with
 135 different sizes, as listed in Table 1. It is worth noting that, as the number of levels increases, the largest portion
 136 occupies the dominant part of the overall model. This indicates that the manufacturing time is significantly reduced
 137 when the mesh grid sizes are comparable to the actual nozzle size.
 138
 139
 140
 141
 142
 143
 144
 145
 146
 147
 148
 149
 150
 151
 152
 153
 154
 155
 156
 157
 158
 159
 160
 161
 162
 163
 164
 165



29 Figure 7: Multiple manufacturers for Happy Buddha. (a)–(d) Internal manufacturing of 1, 2, 3, and 4 levels, respectively. (e) Final model.



50
51
52
53
54
55
56
57
58
59
60
61
62
63
64
65

Figure 8: Multiple-level manufacturing design of the bunny model. (a) Overall manufacturing effect with six levels of material. (b)–(d) Internal manufacturing effect of different levels without the yellow surface, whose accuracy is 0.1mm; the displayed level numbers are 3, 4, and 5 respectively.

Table 1: Volume portion of different manufacturing measure with various levels; '1-level' to '6-levels' represent six types of manufacturing approaches with different size elements.

Comparison	$(3.2mm)^3$	$(1.6mm)^3$	$(0.8mm)^3$	$(0.4mm)^3$	$(0.2mm)^3$	$(0.1mm)^3$
1-level	0	0	0	0	0	100%
2-levels	0	0	0	0	97.74%	2.26%
3-levels	0	0	0	95.90%	2.56%	1.53%
4-levels	0	0	92.34%	4.28%	2.51%	0.87%
5-levels	0	85.56%	7.47%	4.29%	1.81%	0.87%
6-levels	72.40%	13.84%	7.52%	3.56%	1.81%	0.87%

To more intuitively show the advantages of our proposed method, the manufacturing time ratio and CPU time of the bunny are compared, as shown in Fig. 9. The comparison is performed with the traditional FDM method, which uses hot melt material with uniform size. In order to ensure that the comparison test is reliable, the method herein has the same accuracy. It can be observed that the manufacturing time decreases as the number of levels increases. The CPU time of multi-level fabrication is significantly smaller than that of uniform fabrication. From the results, it can be seen that the CPU time decreases as the number of levels increases owing to the efficiency of the multi-level approach.

When the number of levels used is larger than 4, the CPU time increases because the cost of mesh refinement is high.

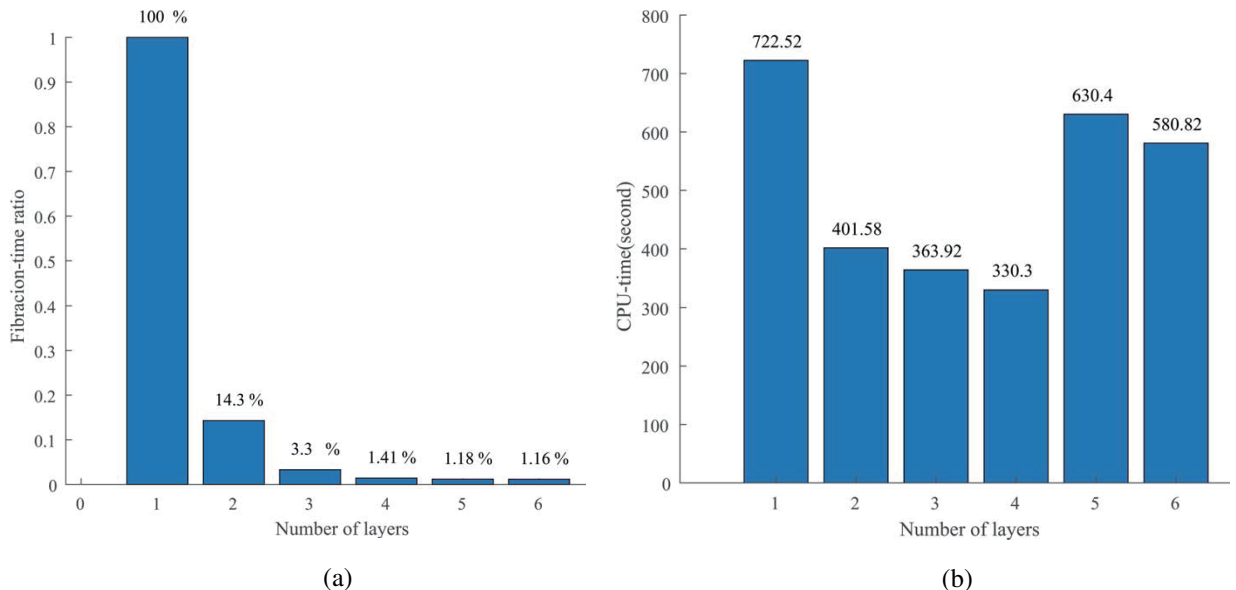


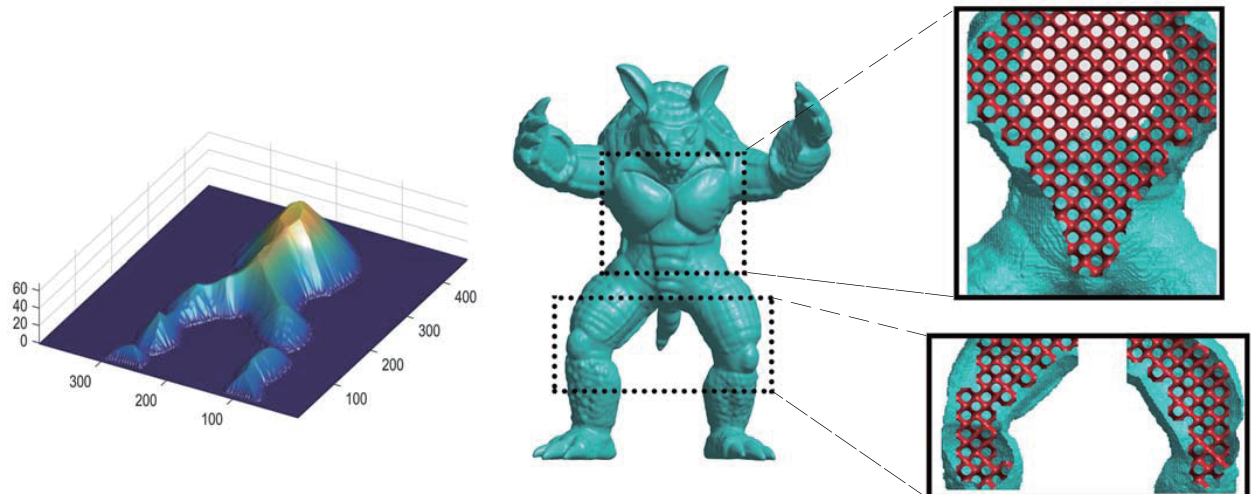
Figure 9: Time comparison of various levels. (a) Relationship between manufacturing-time ratio and number of levels. (b) Relationship between CPU time and number of levels.

Next, fabrication with porous structure is considered. The lightweight structure can be used to replace the in-

1
 2
 3
 4
 5
 6
 7
 8
 9
 10
 11
 12
 13
 14
 15
 16
 17
 18
 19
 20
 21
 22
 23
 24
 25
 26
 27
 28
 29
 30
 31
 32
 33
 34
 35
 36
 37
 38
 39
 40
 41
 42
 43
 44
 45
 46
 47
 48
 49
 50
 51
 52
 53
 54
 55
 56
 57
 58
 59
 60
 61
 62
 63
 64
 65

145 nermost level which has the largest size unit under the condition that the mechanical properties will be guaranteed
 146 [40, 41]. Besides the multi-functional advantages, this further provides a basis for designing structures in the model
 147 with enhanced material efficiency [42]. In addition, lightweight structures reduce model weight based on requirements
 148 [43, 44, 45]. Figure 10 shows the manufacturing effect with the TPMS-P structure with 50% porosity. The volume
 149 is reconstructed from point-cloud data, and the signed distance field is created, as shown in Fig. 10(a). Figure 10(b)
 150 shows the manufacturing effect with four-level materials. The voxel sizes of the first three levels are insufficient;
 151 therefore solid voxels are used to fabricate the cyan part, as shown in Fig. 10. The fourth level is replaced by the
 152 TPMS-P structure with mesh grid size 8. It is clear that the three levels close to the boundary are sufficiently small
 153 to describe the details, and the last level with lightweight elements is a porous scaffold, which decreases material
 154 consumption during fabrication.

155 Figures 11–13 show the multi-level design with the proposed adaptive refinement mesh algorithm. Additionally,
 156 lightweight structures are generated in different models. As shown in Fig. 11(c), the porosity gradient TPMS-P
 157 structure demonstrates the robustness of the algorithm, which is suitable for tissue engineering [46, 47]. Figure 12(c)
 158 shows multi-type composite structures. It is worth noting that the composite structure enables a smooth transition
 159 between TPMS-P and TPMS-G structures, as shown in Fig. 12(d). Figure 13(c) shows multi-scale TPMS-P structure
 160 combination according to the hierarchical algorithm. From these results, it is clear that the proposed method can
 161 function effectively according to different requirements.



49 Figure 10: Simulation of the Armadillo model with combination of TPMS-P structure and solid structure. (a) Mesh plot and (b) manufacturing
 50 design and closed view of the entire model.

51
 52
 53
 54
 55
 56
 57
 58
 59
 60
 61
 62
 63
 64
 65

162 Table 2 presents information on the number of levels, actual model size, ratio and CPU times. Here, the ratio is
 163 computed as the ratio of total manufacturing elements with different nozzles to the total manufacturing elements with
 164 uniform nozzles. The CPU times (in seconds) of the computations are measured on a 3.4 GHz processor with 8 GB
 165 RAM. As can be seen from Table 2, the proposed method achieves high efficiency in terms of both the CPU time and

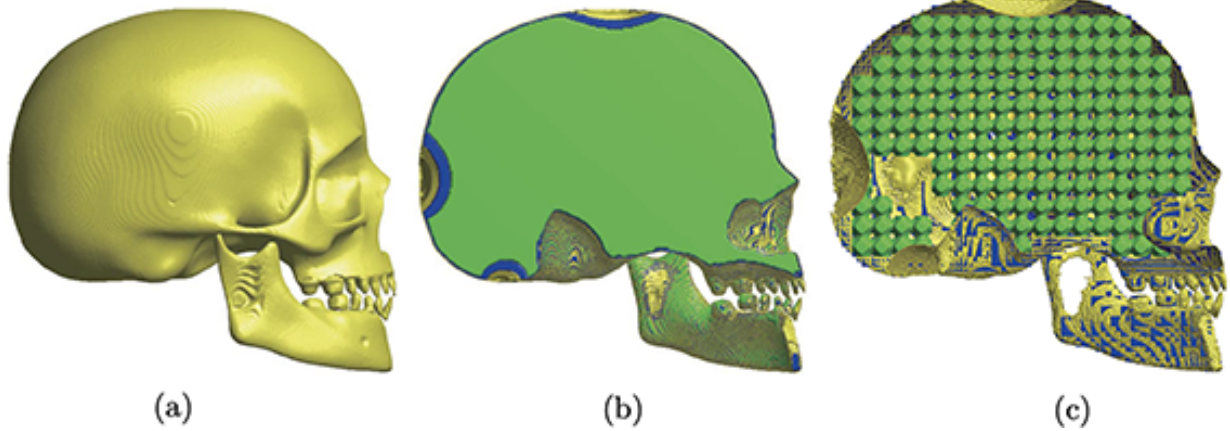


Figure 11: Simulations in the skull model with multi-level design. (a) Complete production design of the model. (b) Closed view in (a). (c) Multi-types structures design effect in the model. TPMS-P and TPMS-G are used in (c). Green, blue and yellow represent the levels with accuracies of 0.1mm, 0.2mm and 0.4mm, respectively.

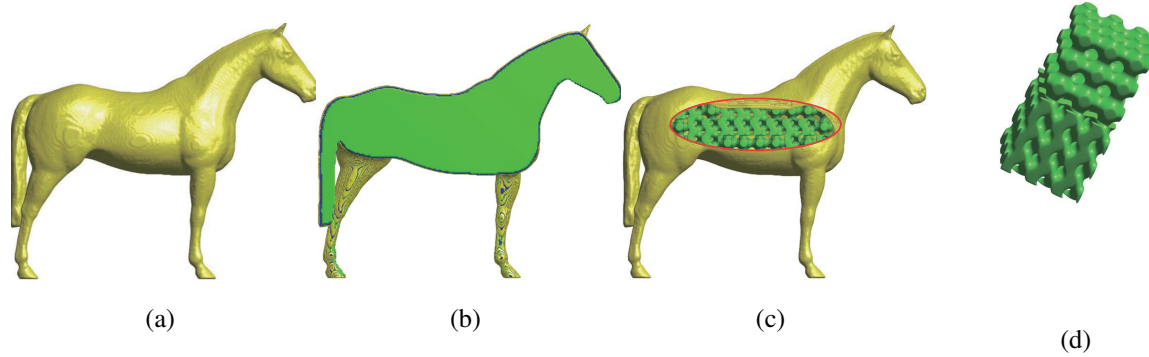


Figure 12: Simulations in the horse model with multi-level design. (a) Complete production effect of the model. (b) Closed view in (a). (c) Multi-types structures design effect in the model. TPMS-P and TPMS-G are used in (c). Green, blue and yellow represent the levels with accuracies of 0.1mm, 0.2mm and 0.4mm, respectively.

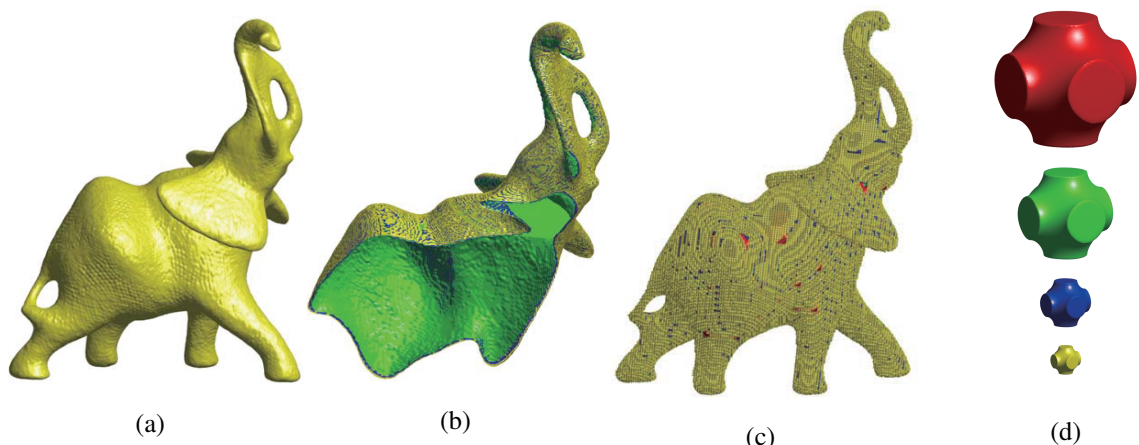


Figure 13: Simulations in the elephant model with multi-level design. (a) Complete production effect of the model. (b) Closed view in (a). Green, blue and yellow represent the levels with accuracies of 0.1mm, 0.2mm and 0.4mm, respectively. (c) Multi-scales TPMS-P structures design effect in the model. (d) TPMS-P structures used in (c).

Table 2: Number of levels, actual model size, ratio and CPU times. Here the ratio is computed as the ratio of the total manufacturing elements with different nozzles to the total manufacturing elements with uniform nozzles.

Case	Level size	Model size((mm) ³)	Ratio	CPU time (s)
Figure 1(b)	4	95.4 × 68 × 44.4	1.46%	318.92
Figure 8(a)	6	98 × 103.2 × 78	0.87%	580
Figure 7(e)	5	44.8 × 105.6 × 44.8	3.18%	249.05
Figure 10	4	45.2 × 53.2 × 41.2	1.80%	70.59
Figure 11(a)	3	71.2 × 103.2 × 96.8	1.35%	465.64
Figure 12(a)	3	28 × 103.2 × 87.2	1.81%	150.61
Figure 13(a)	3	75.2 × 103.2 × 63.2	1.53%	294.44

manufacturing time. Different structures can be designed based on different requirements in the internal area of the model. Furthermore, the use of multiple subspace partitions and multiple accuracy nozzles improves the applicability of the proposed algorithm.

4. Conclusion

In this study, a simple and efficient manufacturing method for additive manufacturing with multiple printing sizes was proposed. Furthermore, porous structures can be used to replace the inside of the model because of their special properties such as high rigidity and lightweight. Multi-scale lightweight structures and porosity gradient structures were generated to further reduce the material weight without affecting the mechanical stability. Various experimental tests were performed to demonstrate the effectiveness and robustness of the proposed method.

Acknowledgment

Y.B. Li is supported by the Fundamental Research Funds for the Central Universities (No.XTR042019005) and the China Postdoctoral Science Foundation (No.2018M640968). B.H. Lu are supported by Shanxi Provincial Science and Technology Planning Project(2017KTZD6-01) and Dongguan University of Technology High-level Talents (Innovation Team) Research Project (KCYCXPT2016003). The corresponding author (J.S. Kim) was supported by Basic Science Research Program through the National Research Foundation of Korea (NRF) funded by the Ministry of Education (NRF-2016R1D1A1B03933243).

Conflict of interests

The authors declare that there is no conflict of interests regarding the publication of this article.

1
2
3 **184 References**
4
5
6
7
8
9
10
11
12
13
14
15
16
17
18
19
20
21
22
23
24
25
26
27
28
29
30
31
32
33
34
35
36
37
38
39
40
41
42
43
44
45
46
47
48
49
50
51
52
53
54
55
56
57
58
59
60
61
62
63
64
65

- [1] D. Han, C. Yang, N.X. Fang, H. Lee, Rapid multi-material 3D printing with projection micro- stereolithography using dynamic fluidic control, *Addit. Manuf.* 27 (2019) 606–615. <https://doi.org/10.1016/j.addma.2019.03.031>.
- [2] S. Sekou, D. Li, B. Lu, Y. Liu, Z. Gong, Y. Liu, Design and fabrication of custom mandible titanium tray based on rapid prototyping, *Med. Eng. Phys.* 26 (2004) 671–676. <https://doi.org/10.1016/j.medengphy.2004.06.001>.
- [3] T. Brajlih, B. Valentan, J. Balic, I. Drstvensek, Speed and accuracy evaluation of additive manufacturing machines, *Rapid Prototyp. J.* 17(2011) 64–75. <https://doi.org/10.1108/1355254111098644>.
- [4] R. Bernhardt, Approaches for commissioning time reduction, *Ind Robot.* 24 (1997) 62–71. <https://doi.org/10.1108/01439919710162719>.
- [5] J.A. Lewis, Direct ink writing of 3D functional materials, *Adv Funct Mater.* 16 (2016) 2193–2204. <https://doi.org/10.1002/adfm.200600434>.
- [6] J.A. Lewis, J.E. Smay, J. Stuecker, J. Cesarano, Direct ink writing of three-dimensional ceramic structures, *J Am Ceram Soc.* 89 (2006) 3599–3609. <https://doi.org/10.1111/j.1551-2916.2006.01382>.
- [7] B.K. Park, D. Kim, S. Jeong, J. Moon, J.S. Kim, Direct writing of copper conductive patterns by ink-jet printing, *Thin Solid Films.* 515 (2007) 7706–7711. <https://doi.org/10.1016/j.tsf.2006.11.142>.
- [8] H. Yang, J.C. Lim, Y. Liu, X. Qi, Y.L. Yap, V. Dikshit, W.Y. Yeong, J. Wei, Performance evaluation of ProJet multi-material jetting 3D printer, *Virtual Phys Prototyp.* 12 (2016) 95–103. <https://doi.org/10.1080/17452759.2016.1242915>.
- [9] F.P.W. Melchels, J. Feijen, D.W. Grijpma, A review on stereolithography and its applications in biomedical engineering, *Biomaterials.* 31 (2010) 6121–6130. <https://doi.org/10.1016/j.biomaterials.2010.04.050>.
- [10] J. Tao, J. Zhang, T. Du, X. Xu, X. Deng, S. Chen, J. Liu, Y. Chen, X. Liu, M. Xiong, Y. Luo, H. Cheng, J. Mao, L. Cardon, M. Gou, Y. Wei, Rapid 3D printing of functional nanoparticle-enhanced conduits for effective nerve repair, *Acta Biomater.* 90 (2019) 49–59. <https://doi.org/10.1016/j.actbio.2019.03.047>.
- [11] F. Guba, U. Tastan, K. Gugeler, M. Buntrock, T. Rommel, D. Ziegenbalg, Rapid prototyping for photochemical reaction engineering, *Chem. Ing. Tech.* 91 (2019) 17–29. <https://doi.org/10.1002/cite.201800035>.
- [12] E. Nguyen, J. Lockyer, J. Erasmus, C. Lim, Improved outcomes of orbital reconstruction with intraoperative imaging and rapid prototyping, *J. Oral Maxil. Surg.* 77 (2019) 1211–1217. <https://doi.org/10.1016/j.joms.2019.02.004>.
- [13] F. Yacob, D. Semere, E. Nordgren, Octree-based generation and variation analysis of skin model shapes, *Mater Manuf Process.* 2 (2018) 52. <https://doi.org/10.3390/jmmp2030052>.
- [14] S.T. Zivanovic, M.D. Popovic, M.D. Vorkapic, M.D. Pjevic, N.R. Slavkovic, An overview of rapid prototyping technologies using subtractive, additive and formative processes, *FME Trans.* 48 (2020) 246–253. <https://doi.org/10.5937/fmet2001246Z>
- [15] J.E. Petrzalka, M.C. Frak, Advanced process planning for subtractive rapid prototyping, *Rapid Prototyp. J.* 16 (2010) 216–224. <https://doi.org/10.1108/13552541011034898>.
- [16] B.E. Kelly, I. Bhattacharya, H. Heidari, M. Shusteff, C.M. Spadaccini, H.K. Taylor, Volumetric additive manufacturing via tomographic reconstruction, *Science* 363 (2019) 1075–1079. <https://doi.org/10.1126/science.aau7114>.
- [17] P. Kulkarni, D. Dutta, An accurate slicing procedure for layered manufacturing, *Comput Aided Des.* 28 (1996) 683–697. [https://doi.org/10.1016/0010-4485\(95\)00083-6](https://doi.org/10.1016/0010-4485(95)00083-6).
- [18] K. Mani, P. Kulkarni, D. Dutta, Region-based adaptive slicing, *Comput. Aided Des.* 31 (1999) 317–333. [https://doi.org/10.1016/s0010-4485\(99\)00033-0](https://doi.org/10.1016/s0010-4485(99)00033-0).
- [19] S. Dehaeck, B. Scheid, P. Lambert, Adaptive stitching for meso-scale printing with two-photon lithography, *Addit. Manuf.* 21 (2018) 589–597. <https://doi.org/10.1016/j.addma.2018.03.026>.
- [20] P.M. Pandey, N.V. Reddy, S.G. Dhande, Slicing procedures in layered manufacturing: a review, *Rapid Prototyp. J.* 9 (2003) 274–288. <https://doi.org/10.1108/13552540310502185>.
- [21] J. Feng, J. Fu, C. Shang, Z. Lin, X. Niu, B. Li, Efficient generation strategy for hierarchical porous scaffolds with freeform external geometries, *Addit Manuf.* 31 (2020) 100943. <https://doi.org/10.1016/j.addma.2019.100943>.

- 1
2
3
4 [22] H. Huang, D. Dean, 3-D printed porous cellulose acetate tissue scaffolds for additive manufacturing, *Addit. Manuf.* 31 (2020) [http://doi.org/10.1016/j.addma.2019.100927](https://doi.org/10.1016/j.addma.2019.100927).
- 5
6 [23] J.H. Parka, J.Y. Parkb, I.C. Namc, M. Ahn, J.Y. Lee, S.H. Choi, S.W. Kimc, D.W. Cho, A rational tissue engineering strategy
7 based on three-dimensional (3D) printing for extensive circumferential tracheal reconstruction, *Biomaterials* 185 (2018) 276–283. [http://doi.org/10.1016/j.biomaterials.2018.09.031](https://doi.org/10.1016/j.biomaterials.2018.09.031).
- 8
9 [24] M. Maruyama, A. Nabeshima, C.C. Pan, A.W. Behn, T. Thio, T. Lin, J. Pajarinen, T. Kawai, M. Takagi, S.B. Goodman, P.P. Yang, The effects
10 of a functionally-graded scaffold and bone marrow-derived mononuclear cells on steroid-induced femoral head osteonecrosis, *Biomaterials*
11 187 (2018) 39–46. <https://doi.org/10.1016/j.biomaterials.2018.09.030>.
- 12
13 [25] Y. Li, S. Guo, Triply periodic minimal surface using a modified Allen-Cahn equation, *Appl. Math. Comput.* 295 (2017) 84–94. [http://doi.org/10.1016/j.amc.2016.10.005](https://doi.org/10.1016/j.amc.2016.10.005).
- 14
15 [26] D.J. Yoo, Computer-aided porous scaffold design for tissue engineering using triply periodic minimal surfaces, *Int. J. Precis. Eng. Man.* 12
16 (2011) 61–71. <https://doi.org/10.1007/s12541-011-0008-9>.
- 17
18 [27] D.J. Yoo, Porous scaffold design using the distance field and triply periodic minimal surface models, *Biomaterials* 32 (2011) 7741–7754.
19 https://doi.org/10.1016/j.biomaterials.2011.07.019.
- 20
21 [28] S. Fujimori, M. Weber, Triply periodic minimal surfaces bounded by vertical symmetry planes, *Manuscripta Math.* 129 (2009) 29–53.
22 https://doi.org/10.1007/s00229-008-0245-0.
- 23
24 [29] J. Klinowski, A.L. Mackay, H. Terrones, Curved surfaces in chemical structure, *Phil. Trans. R. Soc. Lond. A* 354 (1996) 1975–1987.
25 https://doi.org/10.1098/rsta.1996.0086.
- 26
27 [30] E.A. Lord, A.L. Mackay, Periodic minimal surfaces of cubic symmetry, *Current Sci.* 85 (2003) 346–362. <http://www.jstor.org/stable/24108665>.
- 28
29 [31] O. Al-Ketan, M.A. Assad, R.K.A. Al-Rub, Mechanical properties of periodic interpenetrating phase composites with novel architected
30 microstructures, *Compos. Struct.* 176 (2017) 9–19. <https://doi.org/10.1016/j.compstruct.2017.05.026>.
- 31
32 [32] X.Y. Zhang, X.Z. Yan, G. Fang, M. Liu, Biomechanical influence of structural variation strategies on functionally graded scaffolds con-
33 structed with triply periodic minimal surface, *Addit. Manuf.* 32 (2020) 101015. <https://doi.org/10.1016/j.addma.2019.101015>.
- 34
35 [33] J. Liu, Q. Chen, Y. Zheng, R. Ahmad, J. Tang, Y. Ma, Level set-based heterogeneous object modeling and optimization, *Comput. Aided
Des.* 110 (2019) 50–68. <https://doi.org/10.1016/j.cad.2019.01.002>.
- 36
37 [34] Z. Luo, Y. Zhao, A survey of finite element analysis of temperature and thermal stress fields in powder bed fusion Additive Manufacturing,
38 https://doi.org/10.1016/j.addma.2018.03.022.
- 39
40 [35] J.L. Bartlett, X. Li, An overview of residual stresses in metal powder bed fusion, *Addit. Manuf.* 27 (2019) 131–149. [http://doi.org/10.1016/j.addma.2019.02.020](https://doi.org/10.1016/j.addma.2019.02.020).
- 41
42 [36] E. Vespa, N. Nikolov, M. Grimm, L. Nardi, P.H.J. Kelly, S. Leutenegger, Efficient octree-based volumetric SLAM supporting signed-distance
43 and occupancy mapping, *IEEE Robot Autom. Mag.* 3 (2018) 1144–1151. <https://doi.org/10.1109/LRA.2018.2792537>.
- 44
45 [37] L.T. Phuc, M. Seita, A high-resolution and large field-of-view scanner for in-line characterization of powder bed defects during additive
46 manufacturing, *Mater. Des.* 164 (2019) 107562. <https://doi.org/10.1016/j.matdes.2018.107562>.
- 47
48 [38] T.I. Zohdi, Ultra-fast laser-patterning computation for advanced manufacturing of powdered materials exploiting knowledge-based heat-
49 kernels, *Comput. Method Appl. Mech. Eng.* 343 (2019) 234–248. <https://doi.org/10.1016/j.cma.2018.08.040>.
- 50
51 [39] N. Siraskar, R. Paul, S. Anand, Adaptive slicing in additive manufacturing process using a modified boundary octree data structure, *J. Manuf.
Sci. Eng.* 137 (2015) 011007. <https://doi.org/10.1115/1.4028579>.
- 52
53 [40] J. Xu, Y. Wu, L. Wang, J. Li, Y. Yang, Y. Tian, Z. Gong, P. Zhang, S. Nutt, S. Yin, Compressive properties of hollow lattice truss re-
54 inforced honeycombs (Honeytubes) by additive manufacturing: patterning and tube alignment effects, *Mater. Des.* 156 (2018) 446–457.
55 https://doi.org/10.1016/j.matdes.2018.07.019.
- 56
57 [41] Y. He, Y. Zhou, Z. Liu, K.M. Liew, Pattern transformation of single-material and composite periodic cellular structures, *Mater. Des.* 132
58 (2017) 375–384. <https://doi.org/10.1016/j.matdes.2017.07.022>.

- 1
2
3
4 [42] J. Yan, X. Guo, G. Cheng, Multi-scale concurrent material and structural design under mechanical and thermal loads, Comput. Mech. 57
5 (2016) 437–446. <https://doi.org/10.1007/s00466-015-1255-x>.
- 6 [43] H. Wang, Y. Fu, M. Su, H. Hao, A novel method of indirect rapid prototyping to fabricate the ordered porous aluminum with controllable
7 dimension variation and their properties, J. Mater. Process. Tech. 266 (2019) 373–380. <https://doi.org/10.1016/j.jmatprotec.2018.11.017>.
- 8 [44] D. Snelling, Q. Li, N. Meisel, C.B. Williams, R.C. Batra, A.P. Drusczitz, Lightweight metal cellular structures fabricated via 3D printing of
9 sand cast molds, Adv. Eng. Mater. 17 (2015) 923–932. <https://doi.org/10.1002/adem.201400524>.
- 10 [45] W. Wang, T.Y. Wang, Z. Yang, L. Liu, X. Tong, W. Tong, J. Deng, F. Chen, X. Liu, Cost-effective printing of 3D objects with skin-frame
11 structures, ACM Trans. Graph. 2013. <https://doi.org/10.1145/2508363.2508382>.
- 12 [46] D.W. Hutmacher, Scaffolds in tissue engineering bone and cartilage, Biomaterials 21 (2000) 2529–2543. [https://doi.org/10.1016/S0142-9612\(00\)00121-6](https://doi.org/10.1016/S0142-9612(00)00121-6).
- 13 [47] J. Shi, J. Yang, L. Zhu, Z. Li, X. Wang, A porous scaffold design method for bone tissue engineering using triply periodic minimal surfaces,
14 IEEE Access 6 (2018) 1015–1022. <https://doi.org/10.1109/ACCESS.2017.2777521>.
- 15
16
17
18
19
20
21
22
23
24
25
26
27
28
29
30
31
32
33
34
35
36
37
38
39
40
41
42
43
44
45
46
47
48
49
50
51
52
53
54
55
56
57
58
59
60
61
62
63
64
65

Conflict of interest statement :

The authors declare that there is no conflict of interests regarding the publication of this article.

Junseok Kim